In-situ Grown SnO$_2$ Nanospheres on Reduced GO Nanosheets as Advanced Anodes for Lithium-ion Batteries

Zhen Wang,[a, b] Lei Chen,[a, b] Jingjie Feng,[a, b] Shenghong Liu,[a, b] Yang Wang,[a, b] Qinghua Fan,[a, b] and Yanming Zhao*[a, b, c]

Nanostructured tin dioxide (SnO$_2$) has emerged as a promising anode material for lithium-ion batteries (LIBs) due to its high theoretical capacity (1494 mAh g^{-1}) and excellent stability. Unfortunately, the rapid capacity fading and poor electrical conductivity of bulk SnO$_2$ material restrict its practical application. Here, SnO$_2$ nanospheres/reduced graphene oxide nanosheets (SRG) are fabricated through *in-situ* growth of carbon-coated SnO$_2$ using template-based approach. The nanosheet structure with the external layer of about several nanometers thickness can not only accommodate the volume change of Sn lattice during cycling but also enhance the electrical conductivity effectively. Benefited from such design, the SRG composites could deliver an initial discharge capacity of 1212.3 mAh g^{-1} at 0.1 A g^{-1}, outstanding cycling performance of 1335.6 mAh g^{-1} after 500 cycles at 1 A g^{-1}, and superior rate capability of 502.1 mAh g^{-1} at 5 A g^{-1} after 10 cycles. Finally, it is believed that this method could provide a versatile and effective process to prepare other metal-oxide/reduced graphene oxide (rGO) 2D nanocomposites.

Introduction

Recently, lithium-ion batteries (LIBs) have been widely employed in consumer electronics and large-scale energy storage equipments because of their high energy/power densities, and long cycling lifetimes.[1–4] Although graphite exhibits well currently as anode materials for commercial LIBs, its limited theoretical capacity (372 mAh g^{-1}) could not meet the future ever-increasing energy demands. Consequently, intensive research tasks have been concentrated on potential alternative anode materials which could achieve higher reversible capacities.[5]

Metal oxides, especially tin dioxide (SnO$_2$) possessing more than twice the capacity of commercial graphite, have been considered as the promising alternative anode materials for LIBs. Nevertheless, the structure of SnO$_2$ undergoes a dramatic volume expansion during discharging and charging processes, resulting in particle pulverization and rapid capacity-deteriorating, which seriously affects the electrochemical properties. Furthermore, the low electrical conductivity is another inherent shortcoming for its practical applications. Given the above two shortcomings, to produce rational carbon-coated (eg. carbon nanotube,[6] graphene[7,8] or polypyrrole[9]) SnO$_2$ nanoarchitecture such as nanorod,[10] nanotube[11] and hollow nanosphere[12] etc. have been conceived as the most versatile and practical strategy. In particular, graphene-based SnO$_2$ generally shows superior electrochemical properties, benefiting from its high electronic conductivity, excellent specific surface areas and unique mechanical stress. As successful examples, Sun et al. developed an atomic layer deposition (ALD) strategy to deposit SnO$_2$ onto graphene nanosheets (GNS) by heating at 1050 °C, and a capacity of 793 mAh g^{-1} after 150 charge/discharge cycles at 0.1 A g^{-1} can be achieved when using GNS as LIBs anodes.[13] Yang et al. designed graphene-based mesoporous SnO$_2$ (G–M–SnO$_2$) material through in situ growth of SnO$_2$ particles on the graphene surface using CTAB as the template, demonstrating high electrochemical performance (847.5 mAh g^{-1} after 50 cycles at 0.1 A g^{-1} with capacity retention of 77%).[14] Furthermore, the 2D graphene-based SnO$_2$ nanostructures with great effective active sites have become a hot spot of study. That is because 2D nanostructures can not only provide shorter ion-diffusion pathways but also mitigate the enormous volume change and structural strain.[15] Very recently, Mai's group fabricated SnO$_2$ quantum dots@graphene oxide (SnO$_2$ QDs@GO) with homogeneous dispersion and high mass loading of SnO$_2$ (about 87.7%) by a facile hydrothermal route, exhibiting promising performance (a charge capacity of 1121 mAh g^{-1} at a specific current density of 0.1 A g^{-1}) and ultra-long cycling stability (a capacity retention of 86% after 2000 cycles at 2 A g^{-1}).[16] Song and co-workers fabricated 3D rGO/SnO$_2$ hybrid by combining hydrothermal reaction with annealing process at 550 °C under N$_2$ atmosphere. Benefiting from the enhanced transport kinetics of electrons/ions within 3D rGO/SnO$_2$ electrode and structural stability, the composite displayed improved capacity (an initial discharge capacity of

[a] Dr. Z. Wang, L. Chen, J. Feng, S. Liu, Y. Wang, Q. Fan, Prof. Y. Zhao
Department of Physics, South China University of Technology, Guangzhou, 510641, China
[b] Dr. Z. Wang, L. Chen, J. Feng, S. Liu, Y. Wang, Q. Fan, Prof. Y. Zhao
South China Institute of Collaborative Innovation, Dongguan, 523808, P. R. China
[c] Prof. Y. Zhao
Guangdong Provincial Key Laboratory of Advanced Energy Storage Materials, South China University of Technology, Guangzhou, 510640, P. R. China
E-mail: zhaoym@scut.edu.cn

1408 mA h g^{-1} with Coulombic efficiency of 76%) and excellent rate capability (a stabilized capacity of 820 mA h g^{-1} at a high rate of 3 C).[17] However, the metal oxide nanoparticles usually aggregate on the surface of graphene, leading to the capacity decay and poor cycling performance.[18,19] In this regard, it is important to fabricate uniform SnO_2 nanocrystals inbuilt into graphene electrode material to further improve its electrochemical cycling performance.

In this paper, a versatile and facile strategy was designed to fabricate 2D SnO_2-embeded reduced graphene oxide (denoted as 2D SRG) nanosheets as anode materials for LIBs. Compared to other 2D SnO_2 composites,[13,14,16,17,20–25] the 2D SRG composites we prepared have a hierarchical structure where SnO_2 nanoparticles were completely embedded in the 2D reduced graphene oxide (rGO) architecture and uniformly dispersed on the rGO layers. The 2D hierarchical nanostructures can not only shorten ion-diffusion pathways but also moderate the huge volume expansion/shrinkage and structural strain. As a result, the electrode materials achieve a reversible discharge capacity of 1063.4 mA h g^{-1} with high Coulombic efficiency (CE) of 88%
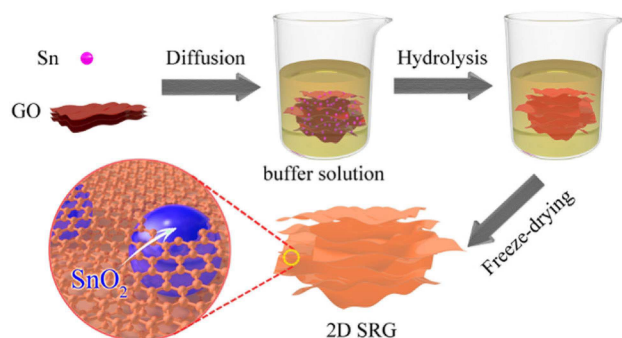
in the first cycle at 1 A g^{-1}. Furthermore, the prepared 2D SRG composites possess an excellent rate capability of 502.1 mA h g^{-1} under even as high as 5 A g^{-1}. Finally, combined with the high electrical conductivity and structural stability, this unique structure also delivers a remarkably specific capacity (1335.6 mA h g^{-1}) with a capacity reservation of 125.6% at 1 A g^{-1} after 500 discharge/charge processes, exhibiting high reversible capacity and extraordinary cycling stability.

Results and Discussion

The formation of 2D SRG nanosheets is demonstrated in Figure 1 and experimental section. Firstly, GO and metal ions are ultrasonically dispersed in an acidic buffer solution under room temperature and metal ions Sn^{2+} is attached onto the GO sheets surface due to its negative charge attraction derived from the large conjugated π bonds. Notably, the hydrolysis reaction of Sn^{2+} is extremely mitigated by adjusting the PH of the buffer solution. Next, the system temperature is quickly increased to 70 °C under strongly magnetic stirring, which will result in nucleation and growth of spheres SnO_2 on the inside of GO to form ultrathin 2D SRG sheets. During this hydrolysis process, Sn^{2+} is oxidized to Sn^{4+}; simultaneously, GO sheets are reduced to rGO. Finally, SnO_2 nanospheres can be obtained by a thermal treatment under air atmosphere, removing the external rGO.

To investigate the morphologies of the 2D SRG nanosheets and SnO_2 nanospheres, the images of scanning electron microscopy (SEM) and transmission electron microscopy (TEM) installed with energy dispersive X-Ray spectroscopy (EDX; Oxford) and selected area electron diffraction (SAED) patterns were displayed in Figure 2. The lowly crystalline hybrid materials 2D SRG possess a size of around 10 μm and the external layer of about several nanometers thickness, as
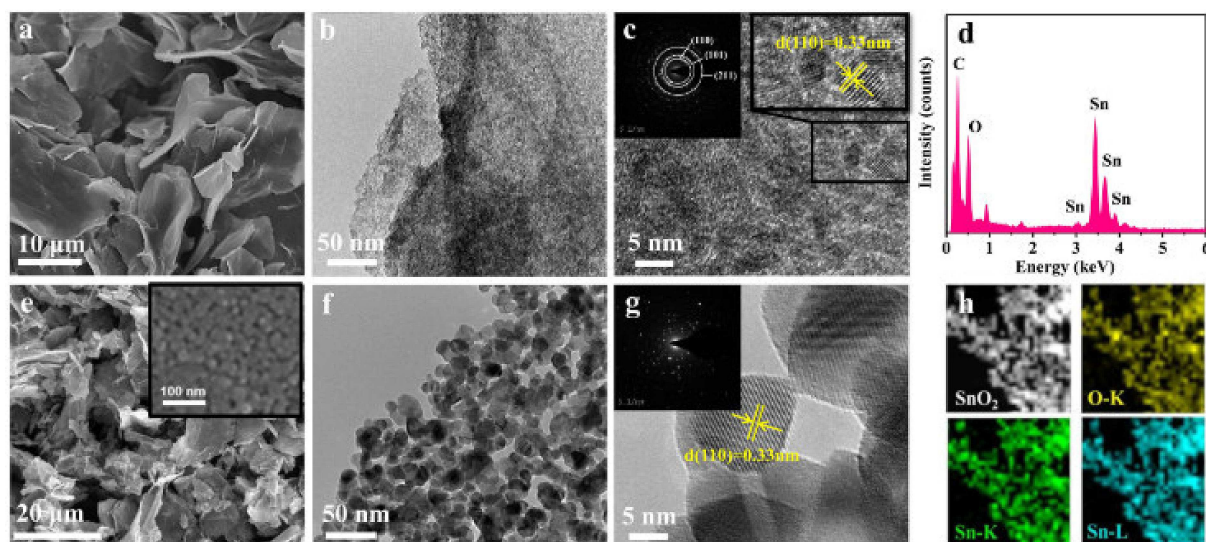

Figure 1. Schematic illustration of the 2D SRG nanosheets fabrication process.

Figure 2. (a) SEM image of 2D SRG composites; (b) TEM image and (c) HRTEM image of the 2D SRG nanosheets (inset: the corresponding SAED pattern) with (d) the corresponding EDX spectrum of 2D SRG; (e) SEM image of SnO_2 (inset: the enlarged SEM image); (f) and (g) TEM images of the SnO_2 nanospheres (inset: the matching SAED pattern); (h) element mapping images of SnO_2.

observed in Figure 2a, demonstrating the formation of GO-coated SnO_2. Figure 2b & c characterize the morphology of 2D SRG samples with the corresponding SAED pattern (inset). The TEM image (Figure 2b) displays that the SnO_2 nanospheres are uniformly embedded in the GO sheets. Meanwhile, the HRTEM image (Figure 2c) shows that SnO_2 nanospheres confined into graphene oxide sheets with a lattice distance of 0.33 nm, corresponding to the (110) face of the SnO_2. From the SAED pattern, the inferiorly crystalline of SnO_2 been identified, which could be the evidence of tetragonal SnO_2, agreeing with the results in Figure 1a. The EDX analysis reveals that the 2D SRG is constituted of tin, oxygen, and carbon elements (Figure 2d). The SEM image (Figure 2e) depicts that the gained SnO_2 is plate-like structure. The TEM images and SAED pattern of the SnO_2 nanospheres presented in Figure 2f & g clearly indicate the characteristics of single crystal, and the average diameter was measured to be 10–20 nm. This lattice distance observed in HRTEM image is 0.34 nm. Also, element mapping images of SnO_2 reveal that Sn and O element were uniformly dispersed (Figure 2h).

Figure 3a demonstrates the powder X-ray diffraction (XRD) patterns of the 2D SRG nanosheets and SnO_2 nanospheres, and all the diffraction peaks can be well indexed as the tetragonal SnO_2 (JCPDS No. 41-1445, space group $P42/mnm$, a = b = 4.738 Å, c = 3.187 Å).[26,27] The (110) peak of graphene oxide could be also apparently observed in the XRD patterns of 2D SRG powders, suggesting that SnO_2 is not deposited on the surface of GO to reduce the degree of graphitization,[28] but

embedded in the GO contributing to the inferior crystallinity. From the TG and DTG curves in Figure 3b, 2D SRG shows 29.4% weight loss from 150 to 800 °C which is assigned to combustion of reduced graphene oxide nanosheets in air, forming CO_2. The N_2 adsorption/desorption isotherms of the 2D SRG was also studied. Figure 3. (a) XRD patterns of GO, SnO_2, 2D SRG, respectively; (b) TG and DTG curves of 2D SRG at temperature from 150 to 800 °C in air; (c) Nitrogen adsorption-desorption isotherm curves of 2D SRG samples (inset: Pore-size distribution plot calculated using the DFT method.); (d) Overall XPS spectrum of 2D SRG nanosheets; (e) High-resolution XPS spectrum of C1s, which can be fitted with four Lorentzian peaks at 284.7, 285.0, 286.3 and 288.6 eV; (f) High-resolution XPS spectra of O 1s and Sn 3d (inset).

It belongs to type IV isotherms with the distinct hysteresis loops, indicating the mesopores and micropores structure of the hybrid materials (Figure 3c).[29] The specific surface area of 2D SRG composites estimated by the BET computational method is 226.9 $m^2 g^{-1}$. The X-ray photoelectron spectroscopy (XPS) general spectra of products 2D SRG nanosheets (Figure 3d) reveal the presence of C, Sn and O elements. The peaks of Sn 3p, 3d, 4d were depicted. The presented peak of the C1s spectrum (Figure 3e) should be devided into four components, corresponding to C—C, C—O, C=O and O=C—O, respectively,[30] mainly attributed to graphene oxide.[31] Additionally, the weak peaks indicate the complete reduction of GO. As shown in the inset of Figure 3f, the components located at 487.7 eV and 496.2 eV are attributed to Sn^{4+}, signing the formation of SnO_2-embeded composites.[32] Similarly, the O1s peak (Figure 3f) can also be further resolved into two components at a binding energy of 531.6 eV and 532.4 eV, which can be assigned to O—C and O—Sn groups.[33]

The electrochemical performance of 2D SRG and SnO_2 as anode materials for LIBs were evaluated, as displayed in Figure 4. Figure 4a and b present the typical discharge/charge profiles of 2D SRG and SnO_2 at 0.1 A g^{-1} in the voltage window of 0.01–3 V, respectively. The 2D SRG exhibits discharge capacities of 1212.3, 1022.8, 1018.9 and 983.4 mA h g^{-1} in the 1st, 2nd, 3th and 10th cycles, respectively. Also, the Coulombic efficiency (CE) of the Figure 4. Discharge-charge curves of (a) 2D SRG composites and (b) SnO_2 measured at the 1st, 2nd, 3th and 10th cycles at 0.1 A g^{-1}; (c) Rate performance of 2D SRG samples at varying current densities from 0.1 A g^{-1} to 10 A g^{-1}. The inset: rate performance of pure SnO_2 samples from 0.1 A g^{-1} to 1 A g^{-1}; (d) Rate capability and (e) representative cycling performances of 2D SRG anodes and nanosphere SnO_2.

2D SRG electrodes reach 98.5% in the 10th cycle. In contrast, the SnO_2 electrodes deliver a lower CE of only 51.0% in the first cycle than that of 2D SRG (about 87.7%). Additionally, it manifests distinctly depressed discharge capacities of 1672.3, 913.0, 870.1 and 661.7 mA h g^{-1} under the same condition, respectively. Furthermore, the 2D SRG electrodes display reversible capacities of 1063.4, 879.7, 768.7, 454.0 and 331.6 mA h g^{-1} with lower specific capacity decay compared with SnO_2 electrodes when the current densities were increased from 0.1 to 0.5, 1, 5 and 10 A g^{-1} (Figure 4c), indicating the superior dynamic electrochemical stability. The rate capability
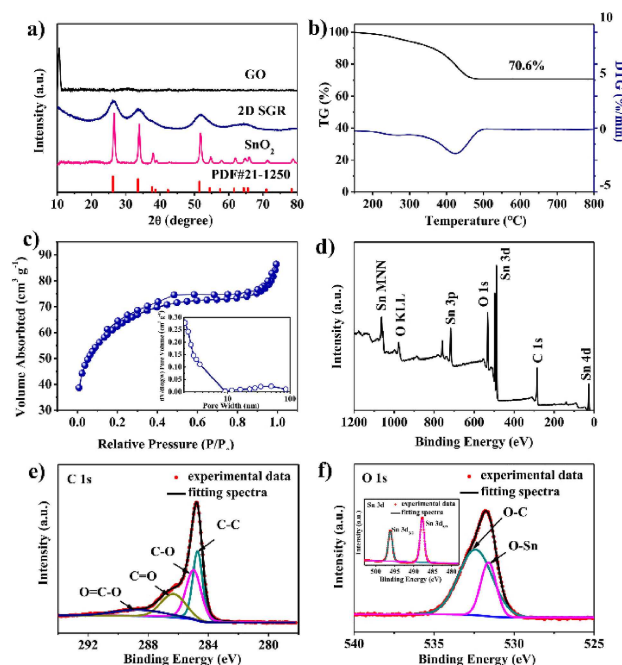

Figure 3. (a) XRD patterns of GO, SnO_2, 2D SRG, respectively; (b) TG and DTG curves of 2D SRG at temperature from 150 to 800 °C in air; (c) Nitrogen adsorption-desorption isotherm curves of 2D SRG samples (inset: Pore-size distribution plot calculated using the DFT method.); (d) Overall XPS spectrum of 2D SRG nanosheets; (e) High-resolution XPS spectrum of C1s, which can be fitted with four Lorentzian peaks at 284.7, 285.0, 286.3 and 288.6 eV; (f) High-resolution XPS spectra of O 1s and Sn 3d (inset).
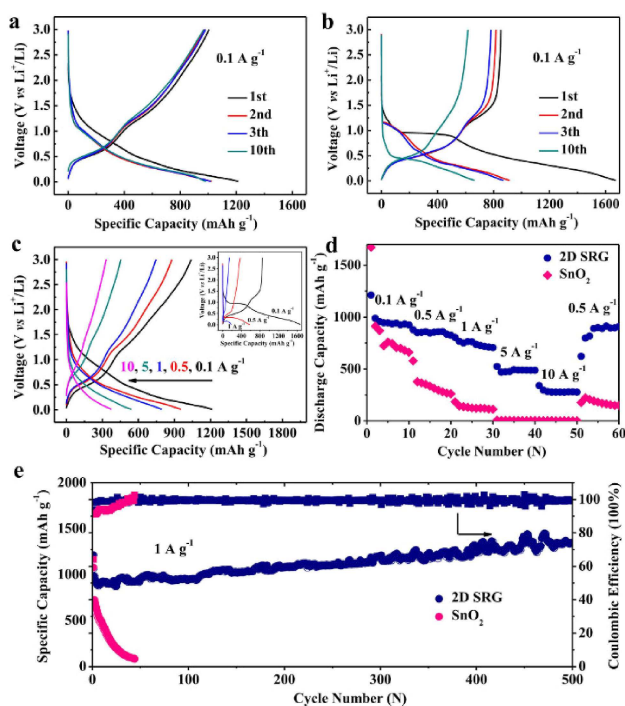
Figure 4. Discharge-charge curves of (a) 2D SRG composites and (b) SnO$_2$ measured at the 1st, 2nd, 3th and 10th cycles at 0.1 A g^{-1}; (c) Rate performance of 2D SRG samples at varying current densities from 0.1 A g^{-1} to 10 A g^{-1}. The inset: rate performance of pure SnO$_2$ samples from 0.1 A g^{-1} to 1 A g^{-1}; (d) Rate capability and (e) representative cycling performances of 2D SRG anodes and nanosphere SnO$_2$.

and long-cycling performance of 2D SRG films and pure SnO$_2$ nanospheres are estimated, as indicated in Figure 4d and e. After the current density was set back from 10 A g^{-1} to 0.5 A g^{-1}, the specific capacity of 2D SRG can still be recovered to 890.5 mAh g^{-1}. The higher lithium-storage properties and cycling performance could only be ascribed to the unique 2D film structure, possessing high electrical conductivity and structural stability. The film-structured 2D SRG electrodes also deliver ultra-high reversible capacity of 1335.6 mAh g^{-1} after 500 cycles at 1 A g^{-1}, which exhibits a higher average capacity of almost 435 mAh g^{-1} compared to the first charging capacity.[34] The TEM images of 2D SRG after 500 cycles have

been performed to investigate the structural stability of 2D SRG (see Fig.S2, Supporting Information). To illustrate the extraordinary long-term cycling properties of the 2D SRG electrodes developed in this study, a summary of the cycling results of similar SnO$_2$/C-based anode materials reported in the last three years is given in Table 1.[6,7,16,35–43] Demonstrably, the result in our study offers so far the superior reversible capacity upon long cycles at a relatively high current density of 1 A g^{-1}. The increased capacity upon cycling is mainly attributed to the following two reasons. On the one hand, the reversible formation and decomposition of an organic polymeric/gel-like layer from the electrolyte, providing interfacial storage for excess lithium-ions, called "pseudo-capacitance-type behavior".[44–47] On the other hand, contact area of the anodes-electrolyte will also increase because of the inevitable collapse and pulverization of SnO$_2$ after cycling, leading to a growing film which can continuously provide extra lithium-storage sites.[44–47]

Figure 5a shows the cyclic voltammogram (CV) curves of the first three cycles of the 2D SRG electrodes under a scan rate of 0.2 mV s^{-1} in the voltage between 0.01 and 3 V (vs. Li/Li$^+$). A loose irreversible reduction peak at 0.68 V belongs to the formation of SEI layer, which was observed only in the initial cycle (Figure 4a). Two large cathodic peaks are detected at 0.96 and 0.20 V in the 2nd and 3th cycles can be ascribed to the Li$_2$O and Li$_{4.4}$Sn alloy formation, respectively.[48] Similarly, during the next two charging process, two obvious oxidation peaks, at 0.58 and 1.25 V, corresponding to reversed phase transition SnO$_2$,[34] indicating the excellent reversibility of the conversion reaction of 2D SRG.

To further evaluate the electrode reaction kinetics in the rate capability, the CV curves of the 2D SRG samples at various scanning rates from 0.2 mV s^{-1} to 1 mV s^{-1} are acquired (Figure 5b). Generally, the current (i) against scan rate (v) follow the formula log$i$ = b × log$v$ + log$a$. Figure 5c shows the linear of logarithm relationship between the peak currents and the square root of scan rates. In this test, the b-values (slopes) for the cathodic peaks 1, 2 and anodic peaks 3, 4 of the 2D SG anodes are 0.75, 0.78 and 0.84, 0.78 respectively, suggesting that fast kinetics in Li-storage reaction is mainly controlled by pseudocapacitive effects.[49] In addition, in the CV plots, the current is composed of capacitive portion (k_1v) and diffusion

Table 1. Comparison of the experimental capacities for reported SnO$_2$ electrodes for storing Li-ions.

| Material	Capacity (mAh g^{-1})	Current density (A g^{-1})	Ref.
SnO$_2$/graphene	700.1 mAh g^{-1}, 80 cycles	0.1 A g^{-1}, 0.01–3 V	35
N-doped SnO$_2$/graphene	803 mAh g^{-1}, 80 cycles	0.1 A g^{-1}, 0.005–2.5 V	36
SnO$_2$/graphene/C	873.2 mAh g^{-1}, 200 cycles	0.2 A g^{-1}, 0.01–3 V	37
SnO$_2$ QDs@GO	~460 mAh g^{-1}, 500 cycles	2 A g^{-1}, 0.01–3 V	16
SnO$_2$/graphene	1073 mAh g^{-1}, 500 cycles	1 A g^{-1}, 0.01–3 V	40
SnO$_2$-N-doped graphene	1041 mAh g^{-1}, 180 cycles	0.2 A g^{-1}, 0.01–3 V	41
Graphene-CNT@SnO$_2$	947 mAh g^{-1}, 100 cycles	0.1 A g^{-1}, 0.01–3 V	6
C/SnO$_2$	915 mAh g^{-1}, 500 cycles	0.5 A g^{-1}, 0.01–3 V	38
SnO$_2$/G-S	970 mAh g^{-1}, 230 cycles	1 A g^{-1}, 0.005–3 V	42
SnO$_2$/Graphene	~1150 mAh g^{-1}, 120 cycles	0.1 A g^{-1}, 0.01–3 V	7
Dual C-SnO$_2$	487.5 mAh g^{-1}, 660 cycles	1 A g^{-1}, 0.01–3 V	43
SnO$_2$/MXene	530 mAh g^{-1}, 500 cycles	1 A g^{-1}, 0.01–3 V	39
2D SRG	1335 mAh g^{-1}, 500 cycles	1 A g^{-1}, 0.01–3 V	This work
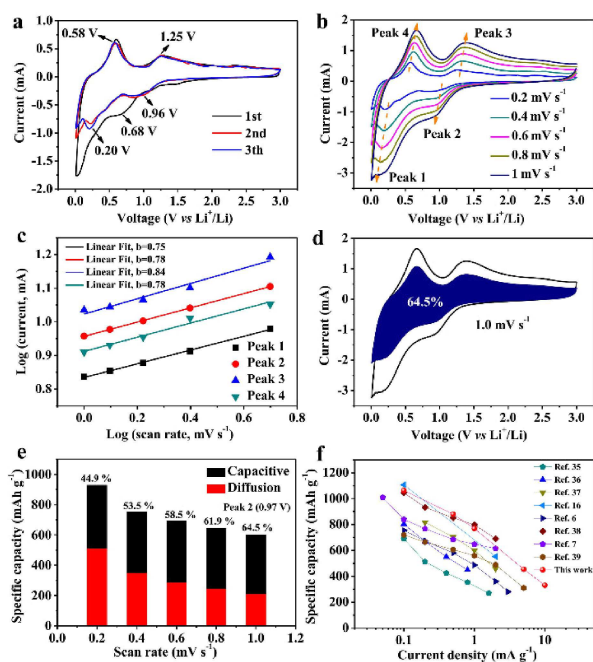
Figure 5. CV curves of 2D SRG electrodes (a) scanned at 0.2 mV s^{-1} and (b) scanned at different scan rates from 0.2 to 1.0 mV s^{-1} and (c) corresponding linear of logarithm relationship between the peak currents (i) and the scan rates (v), (d) capacitive contribution at 1.0 mV s^{-1}, (e) capacitive contribution ratios at diverse rates; (f) comparison of this work with previously reported SnO$_2$-based anode materials.

Figure 6. (a) *In-situ* EIS measurements of the 2D SRG electrodes performed scanned at continous 0.2 mV s^{-1} at various electrochemical states in the first cycle; (b) EIS measurements on a fresh cell and cells after the 1st and 60th cycles for the 2D SRG obtained by applying a sine wave with an amplitude of 5.0 mV over the frequency range 100 kHz 0.01 Hz. The inset is the Nyquist plots of electrodes 2D SG and SnO$_2$ architectures.

portion ($k_2 v^{1/2}$) governed by equation:[50–52] $i(V) = k_1 v + k_2 v^{1/2}$. In Figure 5d, the capacitive contribution of the 2D SRG anodes is 65% at 1.0 mV s^{-1} (blue area). Furthermore, as summarized in Figure 5e, the surface capacitive contribution ratios at the peak 2 (voltage is 0.97 V) are 47.7%, 52.5%, 56.8%, 60.4% and 67.3% at scan rates of 0.2, 0.4, 0.6, 0.8 and 1.0 mV s^{-1}, respectively. High ratios of surface capacitive manifest a short ion-diffusion path during charge and discharge process in the film-structured 2D SRG anodes. As a consequence, fast Li-ion diffusion results in the improved reversibility and rate capability of 2D SRG.[53] Furthermore, the application prospect of 2D SRG anodes in lithium ion full cells has been explored and the assembled 2D SRG //LiCoO$_2$ display initial reversible capacity of 179.1 mA h g^{-1}cathode at 0.2 A g^{-1}cathode in 0.5–4.0 V with only a capacity retention of 48.2% after 50 cycles (Figure S1 in the Supporting Information).

To more vividly illustrate the extraordinary rate performance and electrochemical properties of the 2D SRG electrodes, Figure 5f[6,7,16,35–39] examples the capacities of the similar SnO$_2$-based anode materials reported in the last three years as for comparison. Demonstrably, the result in our study offers the superior reversible capacity at a relatively high current density of 1 A g^{-1}.

To get more details about the solid electrolyte interface resistance (R$_{SEI}$) of the 2D SRG anodes, electrochemical impedance spectra (EIS) was measured at varying electrochemical states, as described in Figure 6. Firstly, Figure 6a presents the *in-situ* EIS plots of the 2D SRG electrodes with various discharging and charging states in the first cycle by
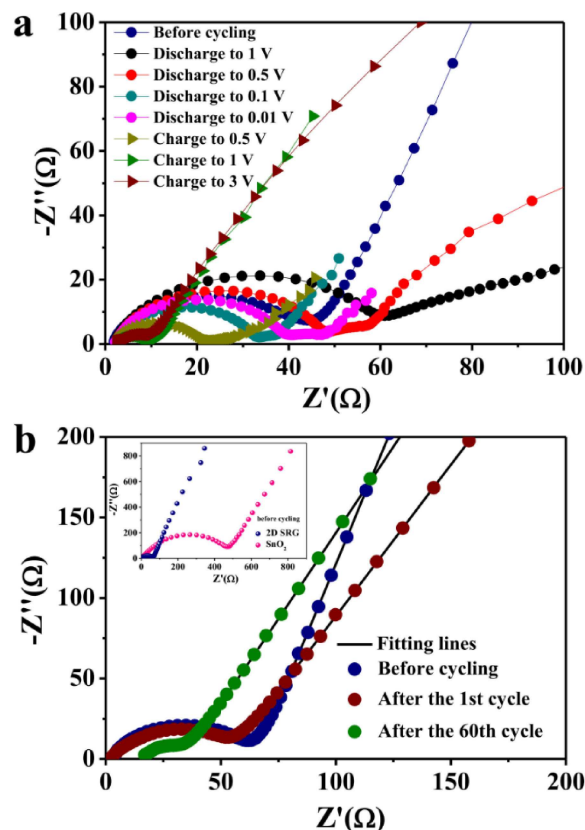
applying an amplitude of 5.0 mV. For the as-prepared 2D SRG nanosheet electrodes in open circuit voltage, only a semi-circle is seen at the high and intermediate frequency regions, manifesting the interfacial impedance between the electrode and the electrolyte.[54,55] When discharged to 0.5 and 0.1 V, two quite depressed semicircles are observed at high-medium frequency region, demonstrating the R$_{SEI}$ and the charge transfer resistance (R$_{ct}$) process, separately. At fully discharging, two improvements of the electrode impedance can be probably attributed to the slow kinetic process. Next, when the electrode is charged to 0.5 and 1 V, respectively, the impedance suffers from a decrease and keeps nearly unchanged after charged to 3 V, indicating that the 2D SRG electrodes are fairly stable upon the lithiation-delithiation process.

Obviously, the diameter of the semicircle for 2D SRG is strongly smaller than that for SnO$_2$ before cycling, which shows that the 2D film composites have much lower impedance than SnO$_2$ partiles, owning to the improved conductivity of carbon coating. Further, Figure 6b identifies the EIS plots of 2D SRG nanocomposites after different cycles. The values of R$_{ct}$ after 1st, 60th cycles and before cycling are 50.88, 19.23 and 51.47 Ω, respectively. The smaller semicircles for 2D SRG after cycling illustrate the facilitated electronic/ionic transport, which is

ascribes to the irreversible lithiated carbon layers,[56] and shortened lengths owning to the minimized size of Sn nanoparticles along with increasing cycles. These above results manifest that this unique composites provide high electronic conductivity, resulting in both excellent cycling properties and high-rate performance.

Conclusions

In summary, we have designed and synthesized a 2D nanosheet SRG material by a simple one-pot solution-based template method. The remarkable rate capability, high reversible capacity and cyclability can be attributed to the unique 2D structure and high electronic conductivity. This unique structure, with fine SnO_2 nanospheres homogeneously encapsulated in rGO nanosheets, effectively promotes the fast transportation of Li^+ ions (or electrons) and suppress the pulverization and aggregation of particle during cycling. As a result, the 2D SRG film electrodes exhibit an initial discharge capacity of 1063.4 $mAh\,g^{-1}$ with CE of 88% at 1 $A\,g^{-1}$. Even at a high current density of 5 and 10 $A\,g^{-1}$, excellent discharge capacity can be still achieved. Moreover, the 2D SRG electrodes also show an extraordinary cycling stability capacity of 1335.6 $mAh\,g^{-1}$ after 500 cycles at 1 $A\,g^{-1}$. Therefore, we believe that the one-pot produce route can be widely adopted to develop other 2D-film-structured metal oxide as anodes toward Li and Na ion batteries in future.

Experimental Section

Synthesis of GO films. GO films were synthesized by Hummer's method on the basis of previous reports.[57]

Synthesis of 2D SRG films. The 2D SRG films were prepared via a feasible template method at 70 °C. Typically, an aqueous dispersion of 8 mL deionized water and 42 mL ethylene glycol were mixed with 0.188 g glycine and 183 μL congregate hydrochloric acid serving as a buffer solution (pH ~ 2.2). Then, 50 mg of GO and 0.934 g of $SnCl_2 \cdot 2H_2O$ were treated by an ultrasonic dispersion in the solution at room temperature for 30 min, leading to metal ions completely attach on the surface of GO. This was followed by vigorous stirring at 70 °C for 4 h. After hydrolysis reaction, the 2D SRG films with 70.6% mass loading of SnO_2 were isolated after centrifugation, washed with excess deionized water to clarify remnant salt and dried in a freezer dryer.

Synthesis of SnO_2 nanospheres. The SnO_2 nanospheres were gained by sintering as-prepared 2D SRG sample at 650 °C for 2 h under air atmosphere.

Structural and electrochemical Characterization. The nanostructures and morphologies of as-obtained 2D SRG composites and SnO_2 nanospheres were studied by X-ray diffraction (XRD; TD-3500), field emission scanning electron microscopy (FE-SEM; Nova Nano-SEM430), high resolution transmission electron microscopy (HRTEM; JEM-2010HR) placed with energy dispersive X-Ray spectroscopy (EDX; Oxford), selected area electron diffraction (SAED), X-ray photoelectron spectroscopy (XPS; Kratos Axis Ultra DLD), Brunner-Emmet-Teller (BET) measurements and Thermogravimetric (TG) analysis. The electrochemical properties were performed using CR2032 coin-type cells. For the examination of 2D SRG and SnO_2, the as-prepared materials, carbon black, and poly (vinylidene

fluoride) (PVDF) were blended at a mass ratio of 8:1:1 into a homogeneous slurry in solvent N-methyl pyrrolidone (NMP) to prepare the working electrodes. The resultant slurry was pressed onto the Cu foil current collector uniformly and dried at 90 °C for 12 h in a vacuum oven, followed by cutting into the wafers 11 mm diameter. The weight of active material of the electrode was about 1.2 $mg\,cm^{-2}$. The electrolyte consisted of a solution of 1 M $LiPF_6$ in a 1:1 mixture of ethylene carbonate and dimethyl carbonate (EC/DMC). The cells were assembled in a glove box full-filled with pure-argon. The cells were galvanostatically discharged/charged over a voltage window of 0.01 V to 3.0 V vs Li^+/Li at a current density of 0.1, 0.5, 1, 5, 10 $A\,g^{-1}$. The electrochemical impedance spectroscopy (EIS) of 2D SRG was carried out by applying an *ac* voltage of 5 mV in the frequency range from 100 KHz to 0.01 Hz on an electrochemical workstation (PGSTAT-30), where cyclic voltammetry (CV) was also collected between 0.01 and 3.0 V at a scanned rate of 0.2 $mV\,s^{-1}$ to 1 $mV\,s^{-1}$.

Acknowledgements

Conflict of Interest

The authors declare no conflict of interest.

[1] M. Armand, J.-M. Tarascon, *Nature* **2008**, *451*, 652–657.
[2] B. Scrosati, J. Garche, *J. Power Sources* **2010**, *195*, 2419–2430.
[3] J. Maier, *Angew. Chem. Int. Ed.* **2013**, *52*, 4998–5026; *Angew. Chem.* **2013**, *125*, 5100–5131.
[4] X. Cao, C. Tan, X. Zhang, W. Zhao, H. Zhang, *Adv. Mater.* **2016**, *28*, 6167–6196.
[5] A. R. Kamali, D. J. Fray, *Rev. Adv. Mater. Sci.* **2011**, *27*, 14–24.
[6] D. Zhou, X. Li, L. Fan, Y. Deng, *Electrochim. Acta* **2017**, *230*, 212–221.
[7] D. Liu, Z. Kong, X. Liu, A. Fu, Y. Wang, Y. G. Guo, P. Guo, H. Li, X. S. Zhao, *ACS Appl. Mater. Interfaces* **2018**, *10*, 2515–2525.
[8] S. Zuo, D. Li, Z. Wu, Y. Sun, Q. Lu, F. Wang, R. Zhuo, D. Yan, J. Wang, P. Yan, *Electrochim. Acta* **2018**, *264*, 61–68.
[9] Z. Cao, H. Yang, P. Dou, C. Wang, J. Zheng, X. Xu, *Electrochim. Acta* **2016**, *209*, 700–708.
[10] L. Qin, J. Xu, X. Dong, Q. Pan, Z. Cheng, Q. Xiang, F. Li, *Nanotechnology* **2008**, *19*, 185705.
[11] Y. Wang, J. Y. Lee, H. C. Zeng, *Chem. Mater.* **2005**, *17*, 3899–3903.
[12] X. W. Lou, C. Yuan, L. A. Archer, *Small* **2007**, *3*, 261–265.
[13] X. Li, X. Meng, J. Liu, D. Geng, Y. Zhang, M. N. Banis, Y. Li, J. Yang, R. Li, X. Sun, M. Cai, M. W. Verbrugge, *Adv. Funct. Mater.* **2012**, *22*, 1647–1654.
[14] S. Yang, W. Yue, J. Zhu, Y. Ren, X. Yang, *Adv. Funct. Mater.* **2013**, *23*, 3570–3576.
[15] J. Liu, X. W. Liu, *Adv. Mater.* **2012**, *24*, 4097–4111.
[16] K. Zhao, L. Zhang, R. Xia, Y. Dong, W. Xu, C. Niu, L. He, M. Yan, L. Qu, L. Mai, *Small* **2016**, *12*, 588–594.
[17] J. I. Lee, J. Song, Y. Cha, S. Fu, C. Zhu, X. Li, Y. Lin, M. K. Song, *Nano Res.* **2017**, *10*, 4398–4414.
[18] F. Schedin, A. K. Geim, S. V. Morozov, E. W. Hill, P. Blake, M. I. Katsnelson, K. S. Novoselov, *Nat. Mater.* **2007**, *6*, 652.
[19] A. Fasolino, J. H. Los, M. I. Katsnelson, *Nat. Mater.* **2007**, *6*, 858.

[20] D. Wang, J. Yang, X. Li, D. Geng, R. Li, M. Cai, T. K. Sham, X. Sun, *Energy Environ. Sci.* **2013**, *6*, 2900–2906.

[21] D. Wang, R. Kou, D. Choi, Z. Yang, Z. Nie, J. Li, J. Liu, *ACS Nano* **2010**, *4*, 1587–1595.

[22] G. Zhu, F. Zhang, X. Li, W. Luo, L. Li, H. Zhang, L. Wang, Y. Wang, W. Jiang, H. K. Liu, S. X. Dou, J. Yang, *Angew. Chem. Int. Ed.* **2019**, *10.*1002.

[23] B. Jiang, Y. He, B. Li, S. Zhao, S. Wang, Y. B. He, Z. Lin, *Angew. Chem. Int. Ed.* **2017**, *56*, 1869–1872; *Angew. Chem.* **2017**, *129*, 1895–1898.

[24] J. Yang, Y. Wang, W. Li, L. Wang, Y. Fan, W. Jiang, W. Luo, Y. Wang, B. Kong, C. Selomulya, H. K. Liu, S. X. Dou, D. Zhao, *Adv. Mater.* **2017**, *29*, 1700523.

[25] D. Ma, Y. Li, H. Mi, S. Luo, P. Zhang, Z. Lin, J. Li, H. Zhang, *Angew. Chem. Int. Ed.* **2018**, *57*, 8901–8905; *Angew. Chem.* **2018**, *130*, 9039–9043.

[26] C. Wang, Y. Zhou, M. Ge, X. Xu, Z. Zhang, J. Z. Jiang, *J. Am. Chem. Soc.* **2009**, *132*, 46–47.

[27] X. Zhou, Y. X. Yin, L. J. Wan, Y. G. Guo, *J. Mater. Chem.* **2012**, *22*, 17456–17459.

[28] J. Yan, Z. Fan, T. Wei, W. Qian, M. Zhang, F. Wei, *Carbon* **2010**, *48*, 3825–3833.

[29] K. S. Sing, *Pure Appl. Chem.* **1985**, *57*, 603–619.

[30] S. Yang, W. Yue, D. Huang, C. Chen, H. Lin, X. Yang, *RSC Adv.* **2012**, *2*, 8827–8832.

[31] A. L. M. Reddy, A. Srivastava, S. R. Gowda, H. Gullapalli, M. Dubey, P. M. Ajayan, *ACS Nano* **2010**, *4*, 6337–6342.

[32] Y. Li, X. Lv, J. Lu, J. Li, *J. Phys. Chem. C* **2010**, *114*, 21770–21774.

[33] Z. Yang, G. Du, Z. Guo, X. Yu, Z. Chen, P. Zhang, G. Chen, H. Liu, *J. Mater. Res.* **2011**, *25*, 1516–1524.

[34] X. Zhou, L. J. Wan, Y. G. Guo, *Adv. Mater.* **2013**, *25*, 2152–2157.

[35] L. Fan, X. Li, B. Yan, X. Li, D. Xiong, D. Li, H. Xu, X. Zhang, X. Sun, *Appl. Energy* **2016**, *175*, 529–535.

[36] Z. Li, G. Wu, S. Deng, S. Wang, Y. Wang, J. Zhou, S. Liu, W. Wu, M. Wu, *Chem. Eng. J.* **2016**, *283*, 1435–1442.

[37] C. Miao, M. Liu, Y.-B. He, X. Qin, L. Tang, B. Huang, R. Li, B. Li, F. Kang, *Energy Storage Mater.* **2016**, *3*, 98–105.

[38] Y. Cheng, Q. Li, C. Wang, L. Sun, Z. Yi, L. Wang, *Small* **2017**, *13*, 1701933.

[39] Y. T. Liu, P. Zhang, N. Sun, B. Anasori, Q. Z. Zhu, H. Liu, Y. Gogotsi, B. Xu, *Adv. Mater.* **2018**, *30*, 1707334.

[40] M. Zhang, Z. Sun, T. Zhang, D. Sui, Y. Ma, Y. Chen, *Carbon* **2016**, *102*, 32–38.

[41] X. Zhou, S. Chen, J. Yang, T. Bai, Y. Ren, H. Tian, *ACS Appl. Mater. Interfaces* **2017**, *9*, 14309–14318.

[42] W. Chen, K. Song, L. Mi, X. Feng, J. Zhang, S. Cui, C. Liu, *J. Mater. Chem. A* **2017**, *5*, 10027–10038.

[43] Q. Wu, Q. Shao, Q. Li, Q. Duan, Y. Li, H. G. Wang, *ACS Appl. Mater. Interfaces* **2018**, *10*, 15642–15651.

[44] Z. Wang, D. Luan, S. Madhavi, Y. Hu, X. W. Lou, *Energy Environ. Sci.* **2012**, *5*, 5252–5256.

[45] P. Poizot, S. Laruelle, S. Grugeon, L. Dupont, J. M. Tarascon, *Nature* **2000**, *407*, 496.

[46] P. L. Taberna, S. Mitra, P. Poizot, P. Simon, J. M. Tarascon, *Nat. Mater.* **2006**, *5*, 567.

[47] J. Jamnik, J. Maier, *Phys. Chem. Chem. Phys.* **2003**, *5*, 5215–5220.

[48] J. C. Lytle, H. Yan, N. S. Ergang, W. H. Smyrl, A. Stein, *J. Mater. Chem.* **2004**, *14*, 1616–1622.

[49] T. Brezesinski, J. Wang, S. H. Tolbert, B. Dunn, *Nat. Mater.* **2010**, *9*, 146.

[50] J. Wang, J. Polleux, J. Lim, B. Dunn, *J. Phys. Chem. C* **2007**, *111*, 14925–14931.

[51] J. B. Cook, H. S. Kim, T. C. Lin, C. H. Lai, B. Dunn, S. H. Tolbert, *Adv. Energy Mater.* **2017**, *7*, 1601283.

[52] V. Augustyn, P. Simon, B. Dunn, *Energy Environ. Sci.* **2014**, *7*, 1597–1614.

[53] P. Simon, Yury Gogotsi, B. Dunn, *Science* **2014**, *343*, 1210–1211.

[54] C. Wang, Y. Xu, Y. Fang, M. Zhou, L. Liang, S. Singh, H. Zhao, A. Schober, Y. Lei, *J. Am. Chem. Soc.* **2015**, *137*, 3124–3130.

[55] M. E. Bhosale, K. Krishnamoorthy, *Chem. Mater.* **2015**, *27*, 2121–2126.

[56] Y. Su, S. Li, D. Wu, F. Zhang, H. Liang, P. Gao, X. Feng, *ACS Nano* **2012**, *6*, 8349–8356.

[57] S. Hummers Jr, S. William, R. E. Offeman, *J. Am. Chem. Soc.* **1958**, *80*, 1339.